

Effect of Plasmonic Au Nanoparticles on Inverted Organic Solar Cell Performance

Jian Wang,[†] Yun-Ju Lee,[†] Arvinder S. Chadha,[‡] Juan Yi,[§] Michael L. Jespersen,^{||} John J. Kelley,^{||} Hue M. Nguyen,[§] Michael Nimmo,[§] Anton V. Malko,[§] Richard A. Vaia,^{||} Weidong Zhou,[‡] and Julia W. P. Hsu^{*,†}

[†]Department of Materials Science and Engineering, University of Texas at Dallas, Richardson, Texas 75080, United States

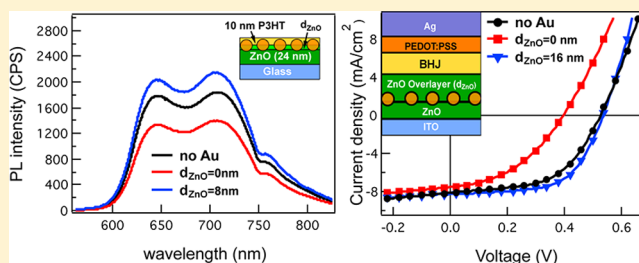
[‡]Department of Electrical Engineering, University of Texas at Arlington, Arlington, Texas 76019, United States

[§]Department of Physics, University of Texas at Dallas, Richardson, Texas 75080, United States

^{||}Air Force Research Laboratory, Wright-Patterson Air Force Base, Ohio 45433, United States

Supporting Information

ABSTRACT: We studied the competition between energy loss due to quenching and enhanced absorption arising from the near-field plasmonic effect of Au nanoparticles (NPs) on the performance of organic solar cells (OSCs), by fabricating inverted architecture OSCs with electron transport layers consisting of an Au NPs monolayer covered by a ZnO overlayer. The distance between Au NPs and a poly(3-hexylthiophene):[6,6]-phenyl-C61-butyric acid methyl ester (P3HT:PCBM) active layer was controlled by systematically varying the ZnO overlayer thickness, and its effect on the absorption spectra, photoluminescence (PL) dynamics, and OSC performance of these films is examined. We found that when P3HT:PCBM is in direct contact with the Au NPs, PL intensity was reduced and the OSC device was shunted with lower values in photocurrent, open circuit voltage, and fill factor. With a thin (8 nm) ZnO overlayer, higher absorption and PL signal were observed, and some OSC device parameters improved, but the short circuit current density remained low. ZnO overlayer thickness greater than 30 nm negated any impact of the AuNPs on the absorption of the active layer. A small (~5%) efficiency enhancement was achieved in the 16 nm ZnO overlayer devices; however, this improvement resulted from increased fill factor rather than photocurrent. Optical field simulation using the finite-difference time-domain (FDTD) method showed that redistribution of the optical field by Au NPs resulted in a 0.6% absorption reduction over the entire P3HT:PCBM active layer.



INTRODUCTION

Since plasmon-enhanced absorption was first shown to improve performance of solar cells,¹ there have been many efforts using noble metal nanoparticles (MNPs) to enhance organic solar cell (OSC) performance.^{2–13} However, the effect of MNPs on OSC performance and the underlying mechanisms remain unresolved, as different groups have found both enhancement and reduction in OSC performance and attributed them to different causes. For example, by blending MNPs in the active layer, Wang et al. reported improved OSC efficiency and attributed the enhancement to reduced resistance and enhanced light absorption from scattering,² while Kim and Carroll suggested the improved performance resulted from increased conductivity but not from higher absorption (i.e., photocurrent).³ In contrast, Xue et al. and Topp et al. reported decreased device performance when MNPs were blended in the active layer.^{4,5} Other researchers have placed MNPs within the poly(ethylene dioxythiophene):poly(styrenesulfonate) (PEDOT:PSS) hole transport layer,^{6,7} between PEDOT:PSS and the anode,^{8–11} or between the active layer and LiF electron transport layer¹² and have attributed the increased photo-

current and OSC efficiency to near-field enhanced active layer absorption.

The size of MNPs determines the dominant mechanism responsible for the plasmonic effect, with near-field enhancement rather than scattering being the primary effect for 5–20 nm MNPs.^{14,15} Because the active layers of OSCs are thin (100–200 nm), smaller MNPs are preferred to minimize shorting between the top and bottom electrodes.¹⁴ Small plasmonic MNPs in OSCs are often fabricated through dewetting and cluster formation of ultrathin evaporated metal films,^{8,12} but such approaches typically generate a wide NP size distribution; thus, the plasma resonance wavelength and intensity are difficult to control. A competition also exists between near-field enhancement of active layer absorption and quenching caused by nonradiative energy transfer to the MNPs,^{16,17} so that the MNPs and the active layer may need to be separated by a thin dielectric spacer to maximize device

Received: September 21, 2012

Revised: November 16, 2012

Published: November 26, 2012

performance. Based on the results of the aforementioned studies, control over MNPs size, morphology, density, separation distance from the active layer, and location within the device architecture are required to clarify the near-field effect contribution to OSC performance.

In this report, we studied inverted OSC performance as a function of the separation distance between 15 nm colloidal Au nanoparticles within a ZnO electron transport layer and the poly(3-hexylthiophene):[6,6]-phenyl-C61-butyric acid methyl ester (P3HT:PCBM) bulk heterojunction (BHJ) active layer. While the design of MNPs with different sizes, geometries, and core compositions (e.g., Cu, Ag, or Au) might have produced more pronounced plasmonic enhancement, our focus in this study was to explore the near-field effect. We chose 15 nm colloidal Au NPs because suspensions of monodisperse NPs can be reproducibly synthesized,¹⁸ their plasmonic resonance frequency overlaps the P3HT absorption band, and their near-field enhancement is larger than the scattering effect. Au NPs with controlled areal density were deposited on top of a thin ZnO film. The distance between the Au NPs and P3HT:PCBM was varied by depositing a second ZnO layer of varying thicknesses to form the electron transport layer of an inverted cell structure.^{19,20} On the basis of this structure, we examined the absorption enhancement, photoluminescence dynamics, optical field distribution in the organic layer, and OSC device parameters.

■ EXPERIMENTAL SECTION

All chemicals were purchased from Sigma-Aldrich and used as received unless otherwise noted. Devices with inverted architecture were fabricated on patterned indium tin oxide (ITO) coated glass substrates (20 Ω /sq, Thin Film Devices). The substrates were cleaned by sonication in solutions of 0.5 vol % surfactant (Aquet) in water and isopropanol (Fisher) for 10 min each, followed by cleaning in a UV-ozone cleaner (Procleaner Plus, Bioforce) for 20 min. ZnO films were deposited by spin-coating at 1000 rpm from an ethanolic solution of 52.5 mM zinc acetate. The sol-gel film was subsequently pyrolyzed on a hot plate in air at 150 °C for 5 min.²¹ After a second coating was cast under the aforementioned conditions, a 24 nm ZnO film was obtained, as determined by ellipsometry. The Au NPs were synthesized according to the well-known citrate reduction method pioneered by Turkevich et al.^{22,23} The as-synthesized Au NPs were stabilized by excess citrate ligands, which etch ZnO in solution. Therefore, ligand exchange was performed on the Au NPs to create a mercaptopropanesulfonate (MPS)-coated surface.²⁴ To minimize ZnO etching, a 1 nM aqueous suspension of the 15 nm Au NPs with pH = 8 and ionic strength of 0.1 mM was prepared by adding 0.14 mM 4-(2-hydroxyethyl)-1-piperazineethanesulfonic acid (HEPES) pH buffer and 0.1 mM NaOH, and the suspension was transferred to a N₂-filled box. The ZnO films were placed in the Au NP suspension for times ranging from 10 to 240 min to deposit Au NP monolayers with different areal densities.^{25,26} Control samples with no Au NPs were prepared by dipping the ZnO films into a pH 8 HEPES buffer solution. After the soaking or deposition of Au NPs, a ZnO overlayer ranging from 0 to 24 nm was spin-coated on top and pyrolyzed at 150 °C. The ZnO or ZnO/Au NPs/ZnO film acts as the electron transport layer in inverted OSCs.

P3HT (Plexcore OS2100, Plextronics) and PCBM (99%, Solenne BV) were used as received. A 1:1 P3HT:PCBM blend

by weight (8 mg/mL each) was prepared in a 1,2-dichlorobenzene and was spin-coated on top of ZnO/(Au)/ZnO films at 600 rpm for 1 min in N₂, dried slowly in a Petri dish over 4 h, and annealed at 110 °C for 10 min.¹⁹ A 50 nm PEDOT:PSS hole transport layer was deposited on top of the P3HT:PCBM from a solution of PEDOT:PSS (Clevios P VP AI 4083, Heraeus Holding GmbH) mixed with 1 wt % of a surfactant (Zonyl FSO-100) by spin-coating at 2000 rpm for 1 min in air, followed by annealing at 120 °C for 10 min in N₂. Finally, silver electrodes (100 nm) were deposited on top using thermal evaporation (Angstrom Engineering) to form OSCs with active area of 0.11 cm².

UV-vis spectra were measured using an Ocean Optics USB 4000 spectrometer with a DT-mini-2-GS light source. ZnO film thickness was measured using a SENTECH SE 800 ellipsometer. The areal density of Au NPs on ZnO film was characterized using a Zeiss Supra 40 field-emission scanning electron microscope (SEM). Photoluminescence (PL) studies were carried out using a microscope-based time-resolved system.²⁷ Samples in a vacuum holder were mounted on the microscope table and excited by 400 nm/120 fs optical pulses at 7.6 MHz repetition rate produced by doubling the fundamental frequency of the Mira 900 laser and followed by pulse-picking (1 out of 10 pulses) via the acousto-optical modulator (NEOS Technologies). Excitation of 100 nW was focused on the sample via 0.6 NA objective, which also ensured a high photon collection efficiency, to obtain PL signals from P3HT film on top of ZnO/Au/(ZnO) structure. The collected emission was passed through a spectrometer and directed either to a CCD camera for PL spectral analysis or to a sensitive photon detector (MicroPhoton Devices MPD 50) for the wavelength-dependent PL lifetime measurements. The PL spectra were averaged over 30 or 60 s and were independent of measuring time. PL decay curves were collected via the time-correlated single photon counting performed on board of Pico300E photon counting hardware (PicoQuant GmbH). The overall time resolution was better than 50 ps. The current density-voltage (J - V) measurements of OSCs were performed in N₂ using a class ACB solar simulator (Newport 67005) with an AM 1.5G filter and a low noise source meter (2635A, Keithley). The surface topography was measured using an Asylum MFP-3D atomic force microscope (AFM). X-ray photoelectron spectroscopy (XPS) of the ZnO/(Au NPs)/ZnO films was carried out using a PerkinElmer 5600 ESCA system with monochromatic Al $K\alpha$ X-ray source (1486.6 eV). All spectra were collected at an angle of 45° to the sample normal, with a pass energy of 58.7 eV and energy step of 0.125 eV.

The finite-difference time-domain (FDTD) simulation was conducted using MIT Electromagnetic Equation Propagation (MEEP), a free software package developed at Massachusetts Institute of Technology.²⁸ Absorption inside P3HT:PCBM was calculated using $A(\lambda) = \omega \text{Im}(\epsilon) \oint |E|^2 dV$, where E is the local simulated electric component of the optical field and V is the volume of the P3HT:PCBM absorbing slab. All optical constants adopted for simulation are presented in the Supporting Information (Figure S1).

■ RESULTS AND DISCUSSION

Fundamental Studies of Near-Field Enhancement. To quantify the near-field effect, it is necessary to reproducibly deposit Au NPs with a controlled areal density on the ZnO film in the OSCs. The Au NP deposition is driven by the attractive

Coulombic interaction between the positively charged ZnO surface and the negatively charged MPS ligands on the Au NPs in solution, while irreversible particle aggregation is prevented by the electrostatic repulsion between nanoparticles with anionic surface ligands. Hence, the deposition and average spacing of Au NPs on the ZnO surface depend strongly on various factors such as pH, ionic strength, Au NPs concentration, and soaking time.²⁵ We found that Au NP concentrations of 1 nM and ionic strengths of 0.1 mM gave a high deposition rate without causing precipitation or aggregation of Au NPs. Second, the reported values for the isoelectric point of ZnO is between pH 8 and 10,²⁹ suggesting pH 8 is ideal for the deposition. Under such conditions, the ZnO film is mostly positively charged but dissolves at a slow rate. After optimizing these parameters, we reproducibly deposited onto ZnO surfaces a monolayer of discrete Au NPs, which remain isolated even after drying (Figure 1 inset).

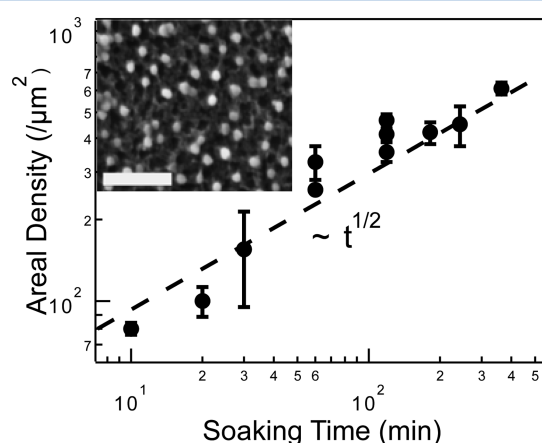


Figure 1. Au NPs areal density on ZnO films versus soaking time for the deposition conditions described in the main text. Dashed line represents areal density proportional to (soaking time)^{1/2}. Inset: SEM image of Au NPs on ZnO surface. The light features in the SEM image are Au NPs. The scale bar represents 200 nm.

The areal density of NPs was approximately proportional to (soaking time)^{1/2} (Figure 1).²⁵ Up to 600/μm² areal density can be reached before dissolution of ZnO was detected by UV–vis absorption. In order to minimize the ZnO dissolution effect, all experiments in this study were performed with less than 400/μm² Au NPs areal density. The adhesion between Au NPs and ZnO was sufficiently strong that no NP aggregation or change in areal density was observed after the deposition of the ZnO overlayer.

We examined the effect of the ZnO overlayer thickness on plasmonic resonance wavelength and intensity of Au NPs using UV–vis spectroscopy.³⁰ Figure 2a shows the UV–vis spectrum for 1 nM Au NPs in an aqueous suspension, showing a plasmon resonance peak at 520 nm. For the Au NPs deposited on top of the ZnO film (Figure 2b, black curve), there is little shift in the plasmon resonance wavelength. We found that as the thickness of the ZnO overlayer (d_{ZnO}) was increased, the Au NPs plasmon resonance peak red-shifted (Figure 2b). This is due to the electric field extending into the surrounding dielectrics.³¹ Since ZnO has higher dielectric constant than air, the total field including the original and the induced fields will resonate at a lower frequency.^{30,32,33} We found that thicker ZnO overlayers resulted in high optical density of the plasmon resonance peak, due to both increased reflection and absorption

as shown by measurement using an integrating sphere (Figure S2). The red shift in the plasmon resonance peak wavelength versus d_{ZnO} is linear for small d_{ZnO} and becomes saturated when the ZnO overlayer becomes thicker than ~30 nm (Figure 2c). In the small d_{ZnO} regime, the electric field from the plasmonic resonance extends into both air and ZnO, while in the thick d_{ZnO} regime, all the near-field electric field is entirely enclosed by the ZnO.³² Hence, we found the effective distance of near-field plasmonic effect to be about 20 nm for 15 nm Au NPs in ZnO sol gel films.

Next, we probed the near-field enhancement effect of Au NPs on the absorption of P3HT films. We expected P3HT film in close proximity to the Au NPs to show the highest absorption enhancement. Thus, we studied the dependence of P3HT absorption on d_{ZnO} for various thicknesses of P3HT films (d_{P3HT} , Figure 2d). To calculate the absorption enhancement ratio, we first integrated the absorbance spectra from 400 to 700 nm and then normalized to the integrated absorbance value without Au NPs. Thus, increased absorption is indicated by an enhancement ratio value of >1. When the P3HT film is very thin (~7 nm, black circles in Figure 2d) and in direct contact with the Au NPs, the enhancement could reach as high as 1.4. For large d_{ZnO} and large d_{P3HT} , the enhancement ratio decreases toward 1. In other words, for thick ZnO overlayers, P3HT mostly resides outside of the near-field enhancement region, as determined from Figure 2c. For thick P3HT, both the diminishing near-field effect and the dominance of bulk absorption decrease the absorption enhancement. Based on these measurements, for a 10 nm ZnO overlayer, a 10% increase in the absorption can be observed in 10 nm P3HT layer.

It is well-known that, when placed in the vicinity of MNPs, fluorescent molecules exhibit enhanced absorption due to near-field effects, but the energy of the excitation can nonradiatively transfer to the metal particles, leading to quenched luminescence.^{16,17} To probe the quenching effect, we investigated the PL spectra and dynamics of 10 nm P3HT films on top of 400/μm² Au NPs with or without a ZnO overlayer. The thickness of P3HT was chosen based on the absorption results in Figure 2d. Figure 3 shows that there is a quenching effect when P3HT film is in direct contact with Au NPs, as indicated by the reduced PL intensity (Figure 3a, red) and shorter PL lifetime (Figure 3b, red) compared to P3HT deposited on top of ZnO without Au NPs (Figure 3, black).^{27,34} By inserting an 8 nm ZnO overlayer between the Au NPs and the P3HT layer, about 17% higher in PL intensity (Figure 3a, blue) is observed, which is consistent with the absorption enhancement found in Figure 2d, suggesting an increased exciton population due to the enhanced local field. The PL lifetime (Figure 3b, blue) is the same as in the case without Au NPs, signifying no additional decay channels.

Application to Inverted P3HT:PCBM Solar Cells. To study the trade off between exciton quenching and near-field enhanced absorption, the performance of inverted OSCs containing ZnO/Au NPs/ZnO electron transport layer with different ZnO overlayer thickness was examined. Since 10 nm thick active layers almost always produce shorted devices, the P3HT:PCBM blend active layer thickness was chosen to be 100 nm. The devices shown in Figure 4 and Table 1 have Au NPs areal density of 200/μm². Figures 4a and 4b show the light and dark J – V curves, respectively, of the control and ZnO/Au NPs/ZnO devices with various ZnO overlayer thicknesses; the structure of devices are shown in Figure 4a, inset. Table 1 gives

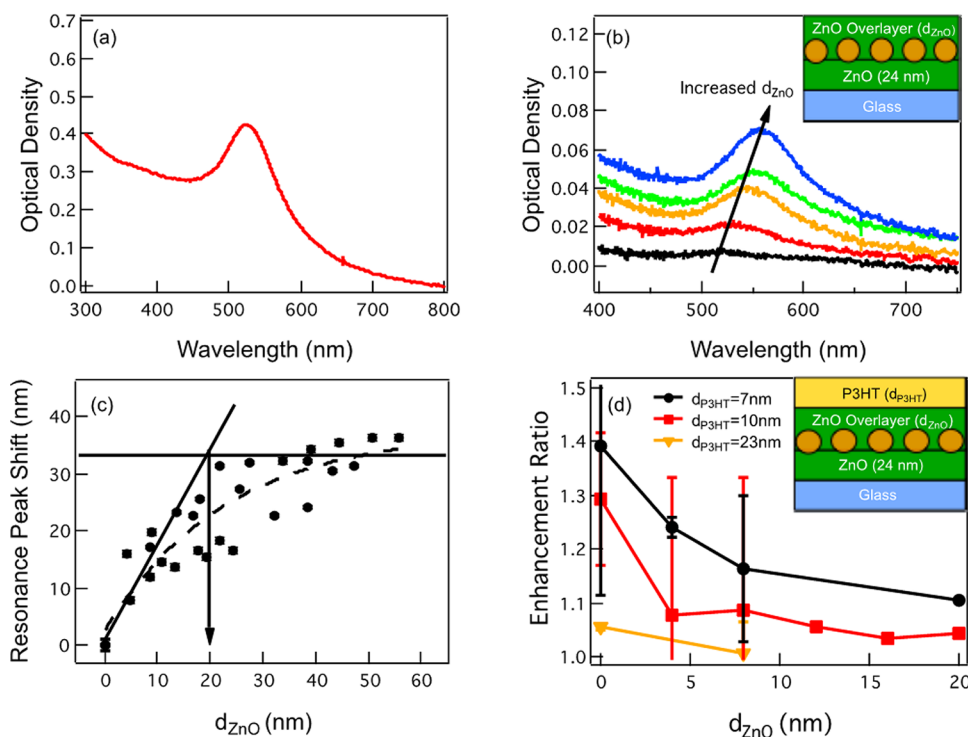


Figure 2. (a) UV-vis absorption spectrum of 1 nM Au NPs in aqueous solution. (b) Optical density of $400/\mu\text{m}^2$ Au NPs (black), with a ZnO overlayer of 4 nm (red), 16 nm (orange), 36 nm (green), and 56 nm (blue). Inset: sample structure. (c) Shift in the plasmonic resonance as a function of ZnO overlayer thickness (d_{ZnO}). The lines are guides to the eye. (d) Absorption enhancement ratio (defined in main text) as a function of d_{ZnO} for different P3HT film thicknesses (d_{P3HT}). Inset: samples structure. Error bars represent standard deviations from different samples with nominally the same d_{ZnO} and d_{P3HT} .

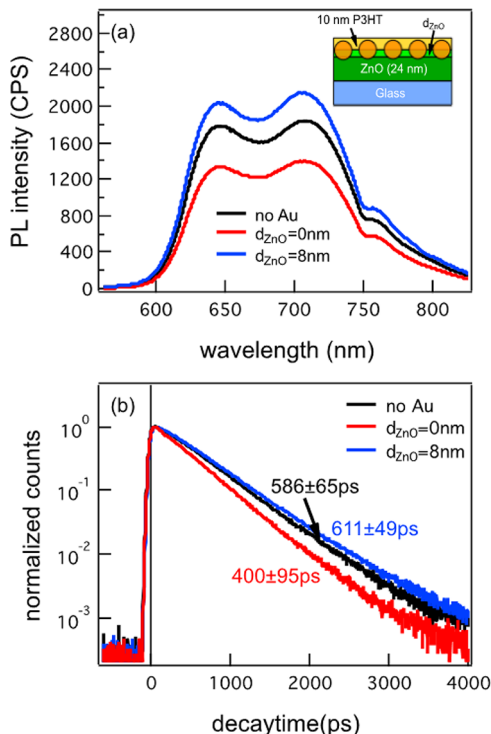


Figure 3. (a) PL spectra and (b) dynamics of a 10 nm P3HT on ZnO without Au NPs (black), directly on top of Au NPs (red), and on top of Au NPs with a 8 nm ZnO overlayer (blue). Inset: structure for PL experiment.

short circuit current density (J_{sc}), open circuit voltage (V_{oc}), fill factor (FF), and power conversion efficiency (PCE) for OSCs with and without Au NPs and with different ZnO overlayer thicknesses. Data from at least 10 diodes were averaged for each device type. For the devices in which active layer in direct contact with the Au NPs (Au NPs only devices), V_{oc} , J_{sc} , and FF all decrease compared to the control. For the 4 nm ZnO overlayer devices, the parameters are higher than the Au NPs only device but are still lower than the control. For thicker ZnO overlayers (8 and 16 nm), V_{oc} and FF become higher than the control. The highest PCE we achieved was 2.35% with a 16 nm ZnO overlayer, which is about 5% higher than control sample at 2.25%. We note that the marginal improved PCE with 16 nm ZnO overlayer corresponds to a decreased series resistance (R_{series} , $7 \Omega \text{ cm}^2$) compared to the control device ($10 \Omega \text{ cm}^2$), which most likely arises from the better electron transport within the ZnO in the presence of Au NPs. In regarding to the plasmonic effect, however, the 16 nm ZnO overlayer devices have about same J_{sc} as the control, indicating that there is no photocurrent enhancement from the near-field effect despite the enhanced absorption. The EQE measurement (Figure S3) showed identical spectra between devices with and without Au NPs.

It should be noted that the shunt resistance (R_{shunt}) values of the Au NPs only, the 4 and 24 nm ZnO overlayer devices are significantly lower than other types of devices, which may account for their poor performances. XPS spectra of the Au NPs sample with a 4 nm ZnO overlayer showed a clear Au 4f signal (Figure 5a). On the basis of the materials parameters and geometry, we estimate the Au 4f to Zn 3p ratio and compare with the experimental results and concluded that the Au NPs are not covered by the thin ZnO overlayer (see Supporting

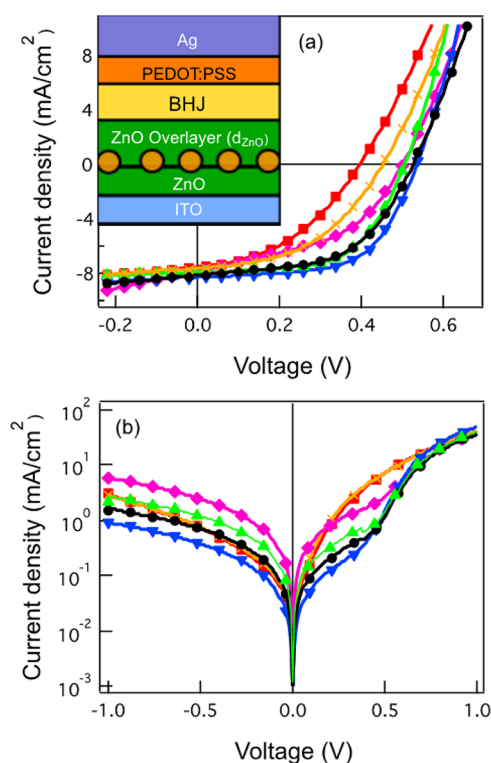


Figure 4. Current density–voltage (J – V) curves of OSCs with various ZnO overlayer on top of Au NPs (a) under simulated 1 sun AM1.5 illumination and (b) in the dark: control (no Au NPs, black circle), Au NPs without ZnO over layer (red square), 4 nm ZnO overlayer (orange cross), 8 nm ZnO overlayer (green triangle), 16 nm ZnO overlayer (blue inverse triangle), 24 nm ZnO overlayer (magenta diamond). Inset: schematic representation of the device structures.

Information). Tapping mode AFM images of the same sample showed protrusions consistent with the topography of 15 nm Au NPs (Figure 5c). Thus, the 4 nm ZnO overlayer devices contain a large amount of exposed Au NPs, leading to direct contact to the active layer similar to the Au NPs only devices. The resulting quenching of excitons may explain the low R_{shunt} and FF of the 4 nm ZnO overlayer and Au NPs only devices. In contrast, the 24 nm ZnO overlayer device completely covered the Au NPs, as indicated by the absence of the Au 4f signal in the XPS spectra (Figure 5b). The AFM image is also much smoother (Figure 5d), suggesting that the spin-coated ZnO overlayer planarized the surface. Thus, the low R_{shunt} of the 24 nm ZnO overlayer device is caused by another mechanism that is currently unknown. Since we have observed this result in many devices made in different runs, we speculate that the cause is related to processing issues when making thicker films.

FDTD Simulation. To understand the apparently contradictory results of enhanced absorption in P3HT without a

corresponding increase in photocurrent, we employed an FDTD method to simulate the electric component of optical field distribution within our P3HT:PCBM OSCs.³⁵ We performed the simulation by considering a plane wave incident perpendicularly to the different layers of an OPV device (z -direction in the simulation setup Figure S4). The schematic of the simulation setup can be found in the Supporting Information (Figure S4). In the simulation, the device structure is uniformly meshed with 2.5 nm grids in all x , y , and z directions. We used a square lattice with a period of 70.7 nm in the x and y directions that contains one Au NP in the unit cell. Periodic boundary conditions were applied to form an infinite square array of Au NPs of a density of $200/\mu\text{m}^2$ in the x – y plane. Shown in Figure 6 is the spatial (x)–spectral (y) distribution of the volume integral of the optical field intensity ($|E|^2$). The x coordinates represent the positions in the light propagating direction in the OPV device while the y coordinates are the wavelength at which the volume integral was evaluated. The solid white lines show the layer separation, and the dashed white lines show the Au NPs position. The spatial–spectral distribution of the optical field intensity $|E|^2$ for a device with 15 nm Au NPs and a 17 nm ZnO overlayer (Figure 6a) is almost identical to that for a control device without Au NPs (Figure 6b). When the intensity difference ((a) – (b)) is normalized to control device, the resulting ratio (Figure 6c) clearly shows the plasmonic resonance at the location of Au NP monolayer. However, the $|E|^2$ slightly decreased within the entire P3HT:PCBM layer after the incorporation of Au NPs, as more clearly seen in the normalized intensity difference integrated from 400 to 700 nm within the cell (Figure 6d). When we calculated the overall absorption for a normally incident plane wave from the optical field distribution using $A(\lambda) = \omega \text{Im}(\epsilon) \oint |E|^2 dV$, where V is the entire volume of the P3HT:PCBM active layer, and integrated to the AM 1.5G spectral intensity over a λ range of 400–840 nm, we found a 0.6% decrease in absorption by the P3HT:PCBM active layer for the device containing Au NPs and a 17 nm ZnO overlayer. Unfortunately, the small change in J_{sc} that is expected for such small decrease in absorption falls well within the experimental uncertainty due to light source nonuniformity and BHJ thickness variation. This simulation results indicate that metal nanostructure located at the front side of OSC might be less favored as the metallic materials could parasitically absorb light. Without perturbing the active layer and introducing additional absorption elements, the more promising approach is to incorporate plasmonic nanostructures at the rear contact, as demonstrated in a recent publication by Niesen et al.¹³

CONCLUSIONS

In summary, we found that monolayers of 15 nm colloidal Au NPs on ZnO with well-characterized areal density generate a

Table 1. Photovoltaic Characteristics of Devices with Various ZnO Overlayer Thickness

	V_{oc} (V)	J_{sc} (mA/cm ²)	FF	PCE (%)	R_{series} (Ω cm ²)	R_{shunt} (Ω cm ²)
control	0.52 ± 0.01	8.04 ± 0.40	0.54 ± 0.04	2.25 ± 0.27	10 ± 2	3152 ± 2594
Au NPs only	0.40 ± 0.00	7.55 ± 0.11	0.42 ± 0.01	1.26 ± 0.02	9 ± 1	948 ± 136
Au NPs + 4 nm ZnO	0.46 ± 0.01	7.63 ± 0.27	0.46 ± 0.01	1.61 ± 0.04	8 ± 2	762 ± 41
Au NPs + 8 nm ZnO	0.52 ± 0.01	7.35 ± 0.53	0.57 ± 0.03	2.19 ± 0.19	8 ± 2	3576 ± 2449
Au NPs + 16 nm ZnO	0.54 ± 0.01	7.88 ± 0.47	0.57 ± 0.04	2.35 ± 0.29	7 ± 1	2172 ± 554
Au NPs + 24 nm ZnO	0.50 ± 0.01	7.86 ± 0.47	0.45 ± 0.05	1.79 ± 0.33	9 ± 2	264 ± 41

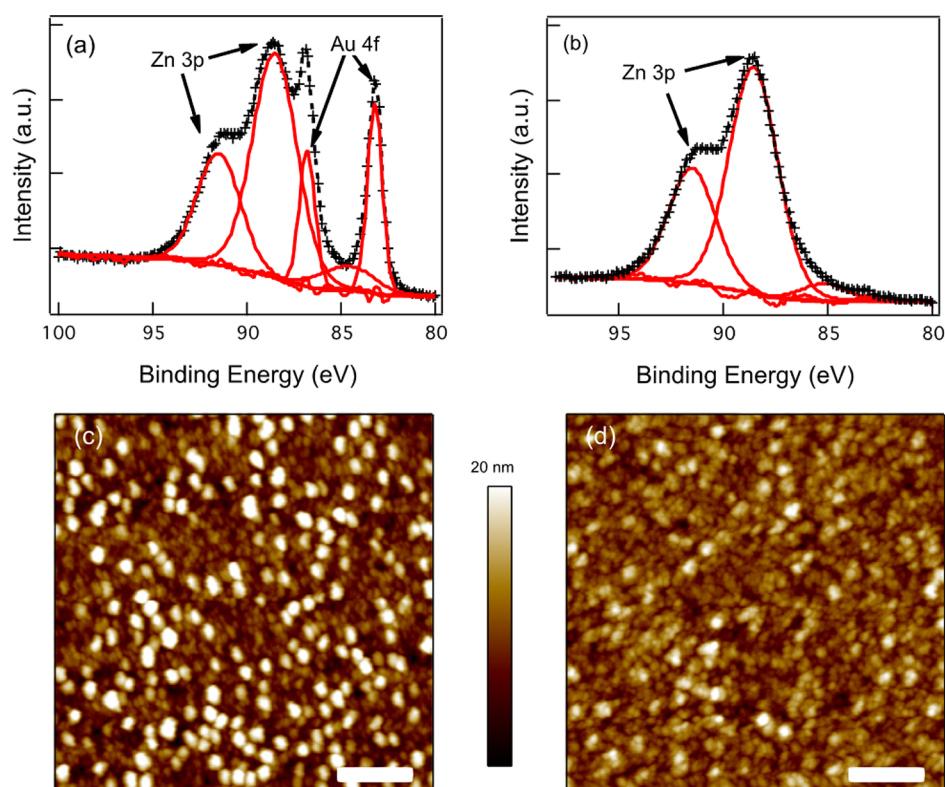


Figure 5. ZnO/Au NPs/ZnO samples with $400/\mu\text{m}^2$ NP areal density and ZnO overlayer thickness of (a, c) 4 nm and (b, d) 24 nm. (a, b) XPS spectra in the Au 4f and Zn 3p region. (c, d) Tapping mode AFM images. Scale bar in AFM images represents 200 nm. RMS roughness = 4.5 nm in (c) and 3 nm in (d).

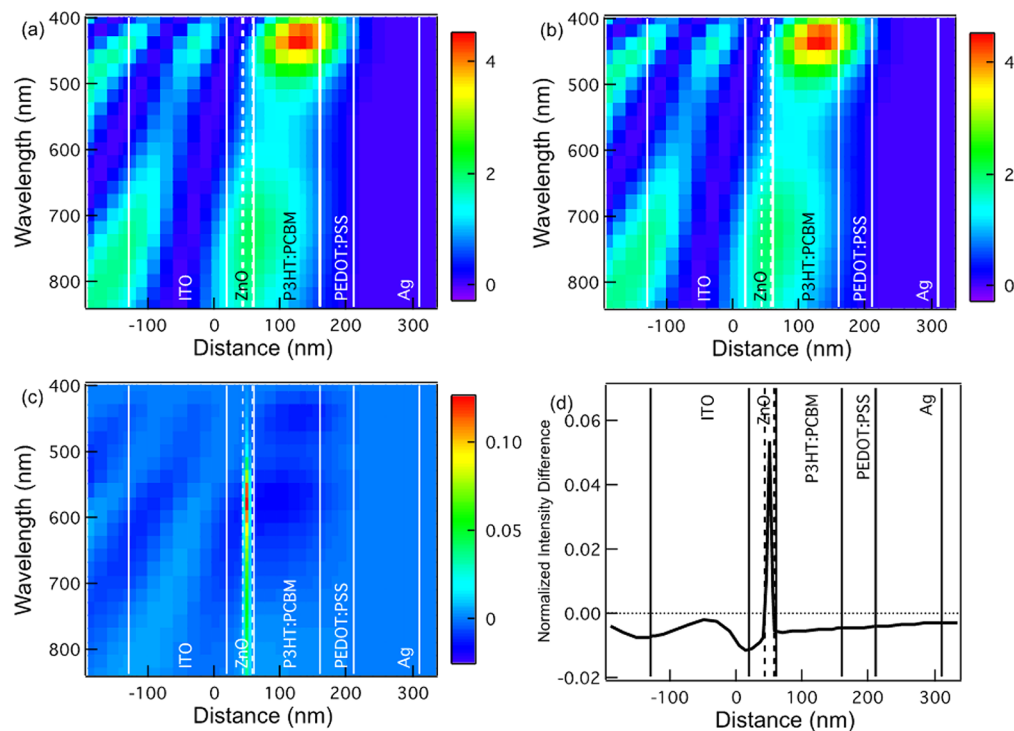


Figure 6. FDTD simulation of optical field intensity ($|E|^2$) on (a) Au NPs with 17 nm ZnO overlayer; (b) no Au NPs with 17 nm ZnO overlayer; (c) normalized intensity difference $((a) - (b))/(b)$; (d) integration of (c) over 400–700 nm. Solid lines: layer separation; dashed lines: Au NPs position. Color scale is the field intensity normalized to incident light.

near-field plasmonic effect on P3HT with a spatial extent of 20 nm. Absorption enhancements were observed in ZnO/Au

NPs/ZnO/P3HT films with combined d_{ZnO} and d_{P3HT} in this range. Both PL measurements and device results indicate that

the active layer needs to be separated from the Au NPs by a ZnO overlayer of ≥ 8 nm to avoid unfavorable exciton quenching. Experimentally, no J_{sc} improvement was observed, but a slight 5% enhancement in efficiency with a 16 nm ZnO overlayer was achieved, which is likely due to improved electron transport. These results are consistent with FDTD simulations that show a redistribution of optical field within the cell by the presence of Au NPs, resulting in a reduction in the optical field intensity in the active layer. These results show that plasmonics are no panacea in enhancing PV performance in every case. A careful evaluation of all factors, including exciton quenching, chemical compatibility, near-field enhanced absorption, morphology perturbation, and contact resistivity change, needs to be carefully considered.

■ ASSOCIATED CONTENT

■ Supporting Information

Reflection/transmission/absorption measurements on ZnO/Au NPs/ZnO structures, the optical constants and simulation setup for FDTD simulations, and the EQE data for devices with and without Au NPs. This material is available free of charge via the Internet at <http://pubs.acs.org>.

■ AUTHOR INFORMATION

Corresponding Author

*E-mail jwhsu@utdallas.edu.

Notes

The authors declare no competing financial interest.

■ ACKNOWLEDGMENTS

This project was supported by Consortium for Nanomaterials for Aerospace Commerce and Technology (CONTACT), University of Texas at Dallas, and Air Force Research Laboratory. J.W.P.H. acknowledges the support from Texas Instruments Distinguished Chair in Nanoelectronics.

■ REFERENCES

- (1) Schaadt, D.; Feng, B.; Yu, E. *Appl. Phys. Lett.* **2005**, *86*, 063106.
- (2) Wang, D. H.; Kim, D. Y.; Choi, K. W.; Seo, J. H.; Im, S. H.; Park, J. H.; Park, O. O.; Heeger, A. J. *Angew. Chem., Int. Ed.* **2011**, *50*, 5519–5523.
- (3) Kim, K.; Carroll, D. *Appl. Phys. Lett.* **2005**, *87*, 203113.
- (4) Xue, M.; Li, L.; de Villiers, B. J. T.; Shen, H.; Zhu, J.; Yu, Z.; Stieg, A. Z.; Pei, Q.; Schwartz, B. J.; Wang, K. L. *Appl. Phys. Lett.* **2011**, *98*, 253302.
- (5) Topp, K.; Borchert, H.; Johnen, F.; Tunc, A. V.; Knipper, M.; Hauff, von, E.; Parisi, J.; Al-Shamery, K. *J. Phys. Chem. A* **2010**, *114*, 3981–3989.
- (6) Chen, F.-C.; Wu, J.-L.; Lee, C.-L.; Hong, Y.; Kuo, C.-H.; Huang, M. H. *Appl. Phys. Lett.* **2009**, *95*, 013305.
- (7) Wu, J.-L.; Chen, F.-C.; Hsiao, Y.-S.; Chien, F.-C.; Chen, P.; Kuo, C.-H.; Huang, M. H.; Hsu, C.-S. *ACS Nano* **2011**, *5*, 959–967.
- (8) Morfa, A. J.; Rowlen, K. L.; Reilly, T. H.; Romero, M. J.; van de Lagemaat, J. *Appl. Phys. Lett.* **2008**, *92*, 139901.
- (9) Kim, S. S.; Na, S. I.; Jo, J.; Kim, D. Y.; Nah, Y. C. *Appl. Phys. Lett.* **2008**, *93*, 073307.
- (10) Lee, J. H.; Park, J. H.; Kim, J. S.; Lee, D. Y.; Cho, K. *Org. Electron.* **2009**, *10*, 416–420.
- (11) Yang, X.; Uddin, A.; Wright, M. *Phys. Status Solidi RRL* **2012**, *6*, 199–201.
- (12) Chen, X.; Zhao, C.; Rothberg, L.; Ng, M.-K. *Appl. Phys. Lett.* **2008**, *93*, 123302.
- (13) Niesen, B.; Rand, B. P.; Van Dorpe, P.; Cheyns, D.; Tong, L.; Dmitriev, A.; Heremans, P. *Adv. Energy Mater.* **2012**, DOI: 10.1002/aenm.201200289.
- (14) Atwater, H. A.; Polman, A. *Nat. Mater.* **2010**, *9*, 205–213.
- (15) Messinger, B.; Vonraben, K.; Chang, R.; Barber, P. *Phys. Rev. B* **1981**, *24*, 649–657.
- (16) Anger, P.; Bharadwaj, P.; Novotny, L. *Phys. Rev. Lett.* **2006**, *96*, 113002.
- (17) Cheng, Y.; Stakenborg, T.; Van Dorpe, P.; Lagae, L.; Wang, M.; Chen, H.; Borghs, G. *Anal. Chem.* **2011**, *83*, 1307–1314.
- (18) Duan, J.; Park, K.; MacCuspie, R. I.; Vaia, R. A.; Pachter, R. J. *Phys. Chem. C* **2009**, *113*, 15524–15532.
- (19) White, M. S.; Olson, D. C.; Shaheen, S. E.; Kopidakis, N.; Ginley, D. S. *Appl. Phys. Lett.* **2006**, *89*, 143517.
- (20) Hau, S. K.; Yip, H.-L.; Baek, N. S.; Zou, J.; O'Malley, K.; Jen, A. K. Y. *Appl. Phys. Lett.* **2008**, *92*, 253301.
- (21) Lee, Y. J.; Davis, R. J.; Lloyd, M. T.; Provencio, P. P.; Prasankumar, R. P.; Hsu, J. W. P. *IEEE J. Sel. Top. Quantum Electron.* **2010**, *16*, 1587–1594.
- (22) Turkevich, J.; Stevenson, P. C.; Hillier, J. *Discuss. Faraday Soc.* **1951**, *11*, 55–75.
- (23) Kimling, J.; Maier, M.; Okenve, B.; Kotaidis, V.; Ballot, H.; Plech, A. J. *Phys. Chem. B* **2006**, *110*, 15700–15707.
- (24) MacCuspie, R. I.; Elsen, A. M.; Diamanti, S. J.; Patton, S. T.; Altfeder, I.; Jacobs, J. D.; Voevodin, A. A.; Vaia, R. A. *Appl. Organomet. Chem.* **2010**, *24*, 590–599.
- (25) Grabar, K.; Smith, P.; Musick, M.; Davis, J.; Walter, D.; Jackson, M.; Guthrie, A.; Natan, M. J. *Am. Chem. Soc.* **1996**, *118*, 1148–1153.
- (26) Jiang, L.; Wang, W.; Fuchs, H.; Chi, L. *Small* **2009**, *5*, 2819–2822.
- (27) Nguyen, H. M.; Seitz, O.; Peng, W.; Gartstein, Y. N.; Chabal, Y. J.; Malko, A. V. *ACS Nano* **2012**, *6*, 5574–5582.
- (28) Oskooi, A. F.; Roundy, D.; Ibanescu, M.; Bermel, P.; Joannopoulos, J. D.; Johnson, S. G. *Comput. Phys. Commun.* **2010**, *181*, 687–702.
- (29) Parks, G. A. *Equilib. Concepts Nat. Water Syst.* **1967**, *67*, 121–160.
- (30) Standridge, S. D.; Schatz, G. C.; Hupp, J. T. *Langmuir* **2009**, *25*, 2596–2600.
- (31) Chu, M.-W.; Chen, C.-H.; de Abajo, F. J. G.; Deng, J.-P.; Mou, C.-Y. *Phys. Rev. B* **2008**, *77*, 245402.
- (32) Evanoff, D.; White, R.; Chumanov, G. *J. Phys. Chem. B* **2004**, *108*, 1522–1524.
- (33) Barber, P. W.; Chang, R. K.; Massoudi, H. *Phys. Rev. B* **1983**, *27*, 7251–7261.
- (34) O'Carroll, D. M.; Hofmann, C. E.; Atwater, H. A. *Adv. Mater.* **2010**, *22*, 1223–1227.
- (35) Zhao, D.; Ma, Z.; Zhou, W. *Proc. SPIE* **2010**, 7772, 777215–1.